

Facile microwave-assisted synthesis of Ce-doped Bi₂O₃ for efficient asymmetric supercapacitors

Xin Tao¹, Mingqi Wei¹, Lianghao Yu¹, Bocheng Zhuang¹, Linlin Zhang¹, Ruilin Zhu¹, Guangzhen Zhao¹, Lu Han¹, Yuanyuan Zhu¹, Huile Jin², and Guang Zhu¹

¹Affiliation not available

²Wenzhou University

October 6, 2023

Abstract

Bi₂O₃ (BT) is considered a fascinating anode material for asymmetric supercapacitors (ASCs) due to its high theoretical capacity, but the low conductivity limits further applications. With this in mind, cerium-doped Bi₂O₃ (Ce-BT) nanoflower spheres were synthesized by a facile and rapid microwave-assisted solvothermal method for ASCs anode materials. It is found that the morphology of BT could be controlled by Ce doping from stacked nanosheets to well-dispersed nanoflowers spheres and producing abundant amorphous regions, thus expediting the ion transport rate. Consequently, When the added Bi to Ce molar ratio is 40:1 (Ce-BT-40), it exhibited a specific capacitance of 721 F g⁻¹ at 0.5 A g⁻¹. Additionally, when fabricating ASCs with as-prepared Ce-BT-40 and CeNiCo-LDH, an energy density of 59.1 Wh kg⁻¹ is provided at a power density of 652 W kg⁻¹. This work not only reveals the mechanism of the effect of Ce doping on the electrochemical properties of BTs but also proposes a rapid synthesis method of Ce-BTs by microwave-assisted solvent method, which provides new insights for building advanced ASCs with high energy density and low cost.

1. Introduction

To date, the contradiction between the rising fossil fuel consumption and insufficient energy supply has escalated, compelling researchers to explore new clean energy sources[1-3]. Supercapacitors (SCs), a novel electrochemical energy storage device, have been extensively studied owing to their ultra-high power density, high durability, and low maintenance cost[4-8]. However, one of the primary drawbacks of SCs is their low energy density, which limits their broader application. Determining the energy density of SCs usually consists of two aspects: the specific capacitance (C) and the voltage window (V) at which the device operates stably. Therefore, boosting C or V is an effective route to further improving energy density. ASCs, a type of SCs with different materials for the anode and cathode, allow for the full utilization of the voltage of both electrodes to expand the operating voltage of the whole cell, thus greatly increasing the energy density[9-12]. To this end, constructing new electrode materials with high specific capacitance and a wide voltage range has become a major scientific challenge. While research on high-performance cathode materials has achieved satisfactory progress, carbon-based nanomaterial anode materials still suffer from the shortcoming of low specific capacitance, severely restricting the further improvement of ASCs' energy densities.

Metal oxides such as MoO₃[13], Bi₂O₃[14], and Fe₂O₃[15] have been demonstrated suitable for use as anode materials. Among them, Bi₂O₃ becomes an ideal material for ASCs anode with the advantages of abundant raw materials, environment friendliness as well as high theoretical capacitance. Nevertheless, the inherent drawback of Bi₂O₃ consists of inferior electrical conductivity and cycling stability, which limits its further applications [16-18]. Conductive materials such as carbon-based materials, have proven to be suitable as buffer layers to effectively reduce the volume change of Bi₂O₃, protect the electrode structure, and enhance

the cycling stability. In addition, carbon material, being highly conductive, serves as the pathway for electron transfer, ensuring rapid electron transfer and enhancing the reversible specific capacitance[19]. Yu et al.[20] employed an organometallic framework derivatization strategy to synthesize carbon-coated Bi_2O_3 ($\text{Bi}_2\text{O}_3@\text{C}$) as the anode material for ASC. Benefiting from the protection of the carbon layer and the ultra-high electrical conductivity, $\text{Bi}_2\text{O}_3@\text{C}$ exhibits specific capacitance (1378 C g^{-1} at 0.5 A g^{-1}). However, due to the inherent low electron conductivity of Bi_2O_3 semiconductor materials, still severely limits the internal electron migration rate.

Heteroatom doping is an effective way to improve the chemical and application properties of materials. Introducing heteroatoms with varying sizes and electronegativity into the original material framework can create structural defects, such as misalignment, bending, or delocalization of the atomic lattice, thereby altering the material's pore structure and generating more electrochemically active sites[21]. Rare earth (RE) doping engineering is an effective method to achieve modulation of the morphological structure and alteration of the electronic structure[22]. This approach significantly enhances electronic conductivity, ion transport rate, and redox activity[23-25]. Among many REs, Ce stands out as the most abundant element with excellent characteristics, such as a large atomic radius and high affinity with oxygen, making it a very promising RE dopant. Xu et al.[26] prepared Ce-doped MoO_3 ($\text{OV-MoO}_3/\text{Ce}$) nanosheets utilized a simple hydrothermal method. Benefiting from the synergistic effects of additional oxygen vacancies arising from Ce doping, high specific surface area, and accelerated electron migration rate. ASCs assembled with Ce-doped OV-MoO_3 as the anode can provide an energy density of 150 Wh kg^{-1} at 800 W kg^{-1} . Therefore, rational Ce doping may serve as an effective approach to enhance the electrochemical performance of Bi_2O_3 . To the best of our knowledge, the utilization of Ce-doped Bi_2O_3 as an anode material in supercapacitors has not been previously reported. In addition, the underlying mechanism of the Ce-doping effect on the electrochemical properties of Bi_2O_3 continues to be unclear. Given this, it becomes essential to synthesize Ce-doped Bi_2O_3 as an anode material for ASCs using a simple method.

Based on the above considerations, we initially synthesized Ce-doped Bi_2O_3 (BT) as an anode material for ASCs using a rapid and fast microwave solvothermal method. On one hand, Ce doping induces a shift in the morphology of Bi_2O_3 from stacked nanosheets to nanoflower spheres, thereby affecting its porosity and specific surface area (SSA). On the other hand, Ce doping enhances the conductivity of BT and reduces its resistance. Consequently, the optimized Ce-BT-40 anode shows high specific capacitance (721 F g^{-1} at 0.5 A g^{-1}) and rate performance (587 F g^{-1} at 10 A g^{-1}). Moreover, with a view to more reasonable capacitance matching, a one-step microwave-assisted hydrothermal method is proposed in this paper to synthesize CeNiCo-LDH. When the ASC is assembled with CeNiCo-LDH as the cathode and Ce-BT-40 as the anode, it provides an energy density of 59.1 Wh kg^{-1} at 652 W kg^{-1} . This work not only elucidates the influence mechanism of RE metals on the electrochemical performance of BT but also introduces a microwave-assisted solvothermal method for the rapid synthesis of electrode materials. These findings provide a novel approach for the development of high energy density and cost-effective ASCs.

2. Results and discussion

Fig. 1a schematically illustrates the preparation process of Ce-BT. In general, Ce-BT was directly synthesized in one step using a microwave-assisted solvothermal method. The synthesis involved bismuth nitrate pentahydrate and cerium nitrate hexahydrate in an acidic mixed polyol. The adjustment of Ce doping in Ce-BT was achieved by controlling the amount of cerium nitrate hexahydrate in the as-fed material. Interestingly, we observed significant changes in the morphological structure of Ce-BT at different Ce contents. The morphology and structure of BT and Ce-BT were characterized using scanning electron microscopy (SEM), as shown in Fig. 1b, c and Fig. S1. Firstly, the BTs (Fig. S1a and d) show a nanosheet-like morphology and are tightly stacked on top of each other. However, at a Ce doping amount of 70:1, we were surprised to find Ce-BT-70 (Fig. S1b and e) gradually transformed from the pristine nanosheet-like morphology to nanoflower spheres, while retaining some regions of nanosheet stacking. When the Ce doping ratio reaches 40:1, Ce-BT-40 exhibits well-dispersed nanoring spherical morphology, as shown in Fig. 1a and b. Furthermore, as the Ce over-doping increases to 10:1, the nanosheet morphology of Ce-BT-10 (Fig.

S1c and f) gradually disappears, and large irregular particles composed of primary nanoparticles take its place. In order to further observe the microstructure of BT and Ce-BT-40, transmission electron microscopy (TEM) was conducted. The TEM images of BT (Fig. S2a and b) show thin nanosheet-like structures. In contrast, Ce-BT-40 (Fig. 1d, e and Fig. S2d and e) shows a nanoflower spherical structure assembled from primary nanosheet units, which is consistent with the SEM results. High-resolution TEM (HRTEM) was employed to observe the lattice streak characteristics of the prepared samples for analyzing the crystal structure composition. The HRTEM image of BT (Fig. S2c) shows two well-defined lattice fringes with calculated lattice spacings of 0.277 nm and 0.185 nm, which closely correspond to the (111) and (220) crystallographic planes of cubic Bi_2O_3 (JCPDS Card No. 27-0052). In contrast, in the HRTEM images of Ce-BT-40 (Fig. 1f and g), a well-defined lattice stripe with a spacing of 0.283 nm was observed, which also corresponds to the (111) crystallographic plane of cubic Bi_2O_3 . This observation suggests that Ce doping promotes an increase in lattice spacing. Notably, a quantity of amorphous regions can be observed in the HRTEM image of Ce-BT-40. This is attributed to the substitution of Bi^{3+} by Ce^{3+} dopant, which leads to the disruption of the original ordering, resulting in the formation of amorphous regions. The homogeneous dispersion of O and Bi elements in BT is shown in the EDX mapping (Fig. S2d). In the Ce-BT-40 sample, however, in addition to Bi and O elements, a substantial amount of Ce is detected, indicating successful doping of Ce into BT, and their distribution is homogeneous without any elemental aggregation.

X-ray diffraction (XRD), X-ray photoelectron spectroscopy (XPS), and nitrogen adsorption/desorption tests were performed to fully characterize the morphology, structure and composition of the prepared samples. As shown in Fig. 2a, the BT sample shows a crystalline phase of cubic Bi_2O_3 (JCPDS Card No. 27-0052), with four prominent diffraction peaks located at $2\theta = 28.5^\circ, 32.2^\circ, 46.2^\circ$, and 54.9° correspond to the (111), (200), (220) and (311) planes, respectively[27]. When Ce was doped into BT, no relevant diffraction peaks attributed to CeO_2 or other Ce-based oxides were observed for any of the three Ce-BT samples, indicating the absence of coexisting Ce-based oxides in the prepared Ce-BT samples. Moreover, the diffraction peak intensities of all Ce-BT samples were lower than those of BT indicating a lower crystalline state. This further demonstrates that Ce-BT contains more amorphous regions due to Ce^{3+} doping. Besides, the valence states of Bi and Ce in the prepared samples have been thoroughly analyzed through XPS testing. Compared with the XPS spectra of the BT samples (Fig. 2b), the three Ce-BT samples not only exhibited peaks attributed to Bi 4f and O 1s but also showed a weak Ce 3d, indicating successful Ce doping in BT. The Bi 4f core-level XPS spectra of BT (Fig. S3a) and the three Ce-BTs (Figs. S3c, 2c, and S3e) show double peaks centered at 164.4 eV and 159.1 eV attributed to Bi 4f_{5/2} and Bi 4f_{7/2}, respectively, suggesting that the Bi ion exists only in a single Bi^{3+} state.[16,28]. The Ce 3d core-level XPS spectra of Ce-BT-70, Ce-BT-40, and Ce-BT-10, respectively, are shown in Fig. S3d, 2d, and S3f, all deconvolved to six peaks corresponding to the Ce 3d_{5/2} and Ce 3d_{3/2} states. These results indicate that the valence state of Ce in Ce-BT samples exists as a mixture of Ce^{3+} and Ce^{4+} (The contents of Ce^{3+} and Ce^{4+} are also labeled in the figures)[29]. In contrast, no distinct peaks were detected in the Ce 3d core-level spectrum of BT (Fig. S3b). Nitrogen adsorption/desorption tests were used to analyze the effect of Ce doping on the SSA and pore size distribution of Bi_2O_3 [30]. In Fig. 2e, all samples exhibit standardized IV adsorption isotherms, which are dominated by mesoporous and macroporous adsorption. H3-type hysteresis loops at relative pressures ranging from 0.45 to 1.0 showed slit-like mesoporous structures with morphologically interconnected and open structures for all samples. This is attributed to the fact that Ce-BT is thin nanosheets cross-linked with each other to form mesoporous structures. The Brunauer-Emmett-Taylor (BET) SSA of BT was calculated to be about $9 \text{ m}^2 \text{ g}^{-1}$ in the range of 0.05-0.3 for the relative pressure P/P_0 . This value is smaller than $12 \text{ m}^2 \text{ g}^{-1}$ for Ce-BT-70 and $15 \text{ m}^2 \text{ g}^{-1}$ for Ce-BT-40, but larger than $8 \text{ m}^2 \text{ g}^{-1}$ for Ce-BT-10. As shown in Fig. 2f, all samples were categorized into two pore sizes, 2-50 nm (mesopore) and greater than 50 nm (macroporous) range, but mesopore adsorption dominated. For the BT samples, the total pore adsorption volume V_t was $0.063517 \text{ cm}^3 \text{ g}^{-1}$, which was smaller than $0.073671 \text{ cm}^3 \text{ g}^{-1}$ for Ce-BT-70 and $0.081762 \text{ cm}^3 \text{ g}^{-1}$ for Ce-BT-40, and larger than $0.057341 \text{ cm}^3 \text{ g}^{-1}$ for Ce-BT-10. Apparently, Ce doping significantly affected the SSA as well as the porosity of BT and showed a tendency of increasing and then decreasing SSA and pore adsorption volume with the increase of Ce doping concentration. This is because a moderate amount of Ce doping causes Ce-BT to shift from stacked nanosheets to well-dispersed nanoflower spheres, while excessive Ce doping leads to the distribution

of the basic nanosheet units into irregular bulk particles, resulting in a decrease in SSA and porosity.

Electrochemical properties are vital for evaluating the practical applications of the as-prepared materials. Hence, we carried out cyclic voltammetry (CV), galvanostatic charge-discharge (GCD), and electrochemical impedance spectroscopy (EIS) tests using the prepared electrodes in a standard three-electrode system. The CV curves of BT and the three Ce-BT electrodes at a scan rate of 10 mV s^{-1} are compared in Fig. 3a. Over the voltage range of -1.2 V to 0 V , all samples similarly showed a pair of distinct redox peaks, confirming the typical Faraday behavior[16,20]. Therefore, we posit that the redox peak is primarily controlled by the redox between the valence states of different Bi, and the Ce dopant does not participate in the redox reaction. Compared with BT, Ce-BT-70, Ce-BT-40, and Ce-BT-10 samples all show stronger peak currents and larger integration areas, and Ce-BT-40 exhibits the best specific capacity, suggesting that rational Ce doping contributes to the increase of charge transfer efficiency as well as electrochemically active sites[31]. Furthermore, GCD tests were performed for all samples at a current density of 0.5 A g^{-1} as shown in Fig. S4a. In the GCD curves, high levels can be observed around -0.55 V and -0.6 V , indicating excellent energy storage characteristics similar to battery behavior. All Ce-BT electrodes have higher discharge times than BT electrodes, among which Ce-BT-40 electrode has the longest discharge time, suggesting its highest discharge specific capacitance. The CV curves of Ce-BT-40 samples at different scan rates from 2 to 30 mV s^{-1} are shown in Fig. 3b. With the increase of scan rate, a pair of distinct redox peaks appeared in the CV curves of all samples, and no significant change in the shape was observed, indicating that the Ce-BT-40 electrode exhibits excellent pseudocapacitance performance and high-rate capability. Additionally, the anodic level peak shifted in the positive direction with increasing scan rate, while the opposite was true for the cathodic peak. This phenomenon may be due to the fact that the rate of electron transport is greater than the migration rate of OH^- ions, leading to a lag in the surface-dominated electrochemical reactions [32,33]. At a scan rate of 2 mV s^{-1} , the specific capacitance value of Ce-BT-40 was calculated to be 709 F g^{-1} , which exceeded that of BT (502 F g^{-1}), Ce-BT-70 (654 F g^{-1}), and Ce-BT-10 (548 F g^{-1}). Meanwhile, the GCD curves of Ce-BT-40 were tested at different current densities, as depicted in Fig. 3c. Notably, when the current densities were set to $0.5, 1, 2, 3, 5,$ and 10 A g^{-1} , the discharge specific capacitances were measured to $721, 692, 675, 648, 615, 592,$ and 587 F g^{-1} , respectively, demonstrating excellent rate performance. Additionally, Fig. 3d presents the discharge specific capacitances of BT and three Ce-BT samples were calculated at different current densities. The discharge specific capacitances of three Ce-BT electrodes were found to be higher than those of the pristine BT electrodes. Notably, Ce-BT-40 showed the highest discharge specific capacity, indicating that appropriate Ce doping is more beneficial in increasing the electrochemical active sites of BT. The rate performance of all the samples is clearly illustrated in Fig. S4b. Specifically, the specific capacitance retention of BT, Ce-BT-70, Ce-BT-40, and Ce-BT-10 was measured to be $75.7\%, 79.3\%, 81.4\%,$ and 78.0% , respectively, at 10 A g^{-1} . Furthermore, the capacitive contribution of the surface reaction process of the Ce-BT-40 electrode was evaluated to reveal the charge storage mechanism. Typically, a power law relationship is observed between the peak current (i) corresponding to the determined potential and the scan rate (v)[34]:

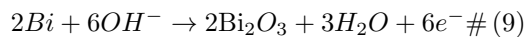
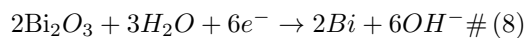
$$i = av^b \quad (6)$$

where a is a constant and b is a power-law index. The b value can be determined from the slope of $\log i$ versus $\log v$ during the redox potential constancy. When the b value is close to 0.5 ; it indicates a diffusion control mechanism, and when it is close to 1 , it signifies a capacitance control mechanism. The b -values of BT, Ce-BT-70, Ce-BT-40, and Ce-BT-10 (Fig. 3e and Fig. S5) are 0.67 and 0.53 ; 0.64 and 0.53 ; 0.64 and 0.53 ; and 0.66 and 0.55 , respectively. These values demonstrate that the capacitance of BT and Ce-BT mainly originated from the diffusion-controlled process on the surface. The charge transfer kinetics and resistance behavior of BT and Ce-BT were investigated using EIS tests. On the one hand, the diameter of the semicircle observed in the high-frequency region of the Nyquist curve represents the magnitude of the charge transfer resistance (R_{ct}), with a larger diameter indicating higher R_{ct} . On the other hand, the slope of the straight line in the low-frequency region reflects the ion diffusion resistance. In Fig. S6a, Nyquist curves of Ce-BT-70, Ce-BT-40, and Ce-BT-10 electrodes exhibited no significant semicircles compared to

the BT electrodes, indicating their R_{ct} were all smaller than BT electrodes. Additionally, the three Ce-BT electrodes also exhibited steeper slopes in the low-frequency region, indicating lower ion diffusion resistance. These findings confirm that Ce doping facilitates the reduction of impedance, accelerates the electron/ion migration rate, and improves BT conductivity. Additionally, we calculate the relaxation time according to the following equation[35]:

$$\tau_0 = \frac{1}{f_0} \# (7)$$

where τ_0 is the relaxation time and f_0 is the frequency at 45° angle. The calculated τ_0 for BT, Ce-BT-70, Ce-BT-40, and Ce-BT-10 were found to be 1800, 22, 18 and 88 ms, respectively (Fig. 3f). The smaller value of τ_0 for Ce-BT-40 indicates the fastest frequency response property, confirming the rapid adsorption and diffusion of electrolyte ions on the Ce-BT-40 electrode. In order to reveal the storage mechanism of Ce-BT-40, we performed ex-situ XRD tests to register the evolution of the crystal structure. As shown in Fig. 3g, in the initial state of the electrode, three characteristic diffraction peaks associated with Bi_2O_3 (JCPDS Card No. 27-0052) were observed. When first discharged to -0.5 V, all diffraction peaks of the Ce-BT-40 electrode gradually weakened and no other new diffraction peaks were detected. When further discharged to -1.1 V, the diffraction peaks attributed to Bi_2O_3 have almost disappeared, and the characteristic diffraction peaks of Bi appear instead (JCPDS Card No. 44-1246), confirming the transition from Bi_2O_3 to Bi. For the first charging process, the presence of both Bi_2O_3 (JCPDS Card No. 41-1449) and Bi was detected in the Ce-BT-40 electrode when the voltage was charged to -0.5 V. This process suggests that Bi is gradually and reversibly converted to Bi_2O_3 . As the voltage was further charged to -0.1 V, the characteristic diffraction peaks of Bi disappeared in the Ce-BT-40 electrode, indicating a complete conversion to Bi_2O_3 . It is important to note that no characteristic diffraction matching the Ce-based compounds was detected in the XRD patterns throughout the entire process. Hence, we argue the following possible reaction process of Ce-BT-40 during the whole charging/discharging process:



Ce does not actively in the electrochemical reactions, yet Ce-doped BT demonstrates superior electrochemical properties. This phenomenon can be attributed to the following two reasons: i) Ce doping into the Bi_2O_3 skeleton causes significant structural changes, leading to the creation of numerous amorphous regions due to misalignment, bending, or delocalization of the original skeleton. This structural modification enhances the electrical conductivity of the material. ii) Ce doping induces a transformation in the BT from stacked nanosheets to well-dispersed nanoflower spheres composed of nanosheet units. This morphological change results in an increased SSA and improved porosity, facilitating more effective electrolyte infiltration. As a consequence, the internal resistance is reduced, and the electron/ion migration path is shortened.

In order to better match the high specific capacitance and wide voltage window of the Ce-BT-40 anode, CeNiCo-LDH material was designed as cathode material. Ce was introduced into NiCo-LDH using a simple microwave-assisted hydrothermal one-step method. The SEM image in Fig. 4a, illustrates the three-dimensional porous morphology of CeNiCo-LDH, with nanosheets interlinked to form the structure. To gain further insight into the microstructure of CeNiCo-LDH, TEM images were obtained. The TEM shown in Fig. 4b further confirmed its cross-linked 3D porous morphology. Furthermore, in the HRTEM image (Fig. 4c), a distinctive lattice stripe with a lattice spacing of 0.476 nm was observed, corresponding to the (100) plane of $\text{Ce}(\text{OH})_3$. This observation confirms the successful incorporation of Ce into the CeNiCo-LDH structure. Powder XRD tests were employed to analyze the crystal structures of NiCo-LDH and CeNiCo-LDH. As depicted in Fig. 4d, the NiCo-LDH samples exhibited distinct characteristic diffraction peaks at $2\theta = 11.2^\circ, 22.5^\circ, 33.5^\circ, 34.2^\circ, 38.5^\circ$, and 45.5° , which correspond to the (003), (006), (101), (012), (104) and (015) planes, respectively[36]. Furthermore, the XRD pattern of CeNiCo-LDH shows two diffraction peaks at 16.2°

and 28.7° that are considered to be the (100) and (101) planes of $\text{Ce}(\text{OH})_3$ [37]. XPS tests were performed to analyze the chemical composition and surface electronic states of the CeNiCo-LDH material. The survey spectrum of CeNiCo-LDH (Fig. 4e) confirms the presence of Ce, Ni, Co, and O. The core-level XPS spectra of Ce 3d (Fig. 4f) reveal the valence state of Ce in the Ce-BT showing a combination of Ce^{3+} and Ce^{4+} states[38]. Regarding the Ni 2p core-level XPS spectra (Fig. S7a), two distinct peaks were detected at 855.4 eV and 872.9 eV, corresponding to the +2 oxidation state of Ni. Additionally, two origin peaks appeared near 874.6 eV and 856.5 eV, corresponding to the oxidation state of Ni^{3+} [39]. Fig. S7b displays the core-level XPS spectra of Co 2p orbitals, with the two dominant self-selected orbital coupling peaks located at 796.7 eV and 780.9 eV, representing the +3 oxidation state of Co $2p_{3/2}$ and Co $2p_{1/2}$, respectively[39]. In the high-resolution XPS spectra of O 1s (Fig. S7c), four peaks were observed at 532.6 eV, 531.4 eV, 531 eV, and 529.6 eV, corresponding to oxygen vacancies, intercalated water molecules, metals bound to hydroxides, and metals bound to oxides, respectively. The prepared NiCo-LDH and CeNiCo-LDH materials were subjected to electrochemical testing in a typical three-electrode setup using a 6 M KOH electrolyte to assess their application as electrodes. Fig. 4g demonstrates the CV curves of NiCo-LDH and CeNiCo-LDH at a scan rate of 10 mV s^{-1} . Obviously, both NiCo-LDH and CeNiCo-LDH exhibit the same curve shape, indicating their energy storage mechanisms are similar. Compared with NiCo-LDH, CeNiCo-LDH exhibits a larger curve area, indicating a larger specific capacitance. In addition, the GCD curve shown in Fig. 4h further confirms the higher discharge specific capacitance of CeNiCo-LDH. For the CeNiCo-LDH electrode, we also collected CV curves for scan rates ranging from $5\text{-}100 \text{ mV s}^{-1}$ (Fig. S8a). As the scan rate increases, all the curves exhibit a distinct pair of redox peaks, and their shapes remain unchanged, indicating excellent pseudocapacitance characteristics and high-rate performance. Additionally, the GCD curves of CeNiCo-LDH electrodes in the current density range of $1\text{-}20 \text{ A g}^{-1}$ further confirm their exceptional pseudocapacitance properties. To facilitate a clear comparison of the specific capacitance and rate performance between NiCo-LDH and CeNiCo-LDH, we calculated the specific capacitance at different current densities, as depicted in Fig. 4i. The discharge specific capacitances of NiCo-LDH were measured to be 743, 731, 704, 682, 646, 631, and 601 F g^{-1} at current densities of 1, 2, 3, 5, 10, and 20 A g^{-1} , respectively. In contrast, the discharge specific capacitances of CeNiCo-LDH were significantly higher at 1042, 978, 938, 877, 796, 757, and 726 F g^{-1} , respectively. The remarkable difference in discharge specific capacitance between CeNiCo-LDH and NiCo-LDH confirms that the introduction of Ce is beneficial in enhancing the electrochemical performance of NiCo-LDH.

To further validate the potential practical applications of Ce-BT-40, we constructed an ASC using Ce-BT-40 as the anode, CeNiCo-LDH as the cathode, and 6 M KOH as the electrolyte (Fig. 5a). Based on the CV curves of Ce-BT-40 and CeNiCo-LDH (Fig. 5b), it is theoretically feasible to fabricate an ASC with an operating voltage of 1.65 V. Additionally, the CV curves obtained by setting a series of voltage ranges (Fig. S9) demonstrate that the ASC device can stably operate within the voltage range of 0-1.6 V. The ASC device exhibits stable operation within the voltage range of 0-1.6 V. Moreover, the CV curves of the ASC device recorded over a scan rate range of $10\text{-}100 \text{ mV s}^{-1}$ are displayed in Fig. 5c, and all CV curve shapes remain well-maintained. This observation indicates excellent rate performance and rapid ion adsorption/desorption kinetics. To provide a more visual representation of the rate performance, we calculated the specific capacitance values at different scan rates, as illustrated in Fig. S10a. Specifically, the specific capacitance of ASC was 189 F g^{-1} at a scan rate of 10 mV s^{-1} and 117 F g^{-1} at 100 mV s^{-1} , with a retention rate of 61.9%. In addition, the GCD curves of ASC in the current density range of $1\text{-}10 \text{ A g}^{-1}$ (Fig. S10b) confirm this excellent rate performance. The assembled Ce-BT-40//CeNiCo-LDH ASC device, with a voltage window of 1.6 V and high specific capacitance, shows promising potential for achieving high energy density. As depicted in Fig. 5d, the device provides 59.1 Wh kg^{-1} at 652 W kg^{-1} . In addition, when the power density was increased to 10.5 kW kg^{-1} , the energy density can still be maintained at 26.1 Wh kg^{-1} . Most notably, as-assembled ASC are still in the leading position compared to previously reported Bi_2O_3 -based ASCs, such as Bi_2O_3 //AC ($1008.67 \text{ W kg}^{-1}$, 18.24 Wh kg^{-1})[40], Bi_2O_3 @C//NiCo-LDH (807 W kg^{-1} , 49 Wh kg^{-1})[20], $\text{Mn-Bi}_2\text{O}_3$ //AC (750 W kg^{-1} , 49.4 Wh kg^{-1})[17], and $\text{h-Bi}_2\text{O}_3$ @C//Ni/Co-MOF (1125 W kg^{-1} , 47 Wh kg^{-1})[41], NiCo_2O_4 @ Bi_2O_3 @C//AC (800 W kg^{-1} , 24 Wh kg^{-1})[31], Bi_2O_3 // CO_3O_4 (1225 W kg^{-1} , 38.5 Wh kg^{-1})[42], and BBMO-6//AC (1703.3 W kg^{-1} , 16.7 Wh kg^{-1})[33]. To further demonstrate

the practicality of the ASCs we fabricated, the combination of the two ASCs in series effectively powers two red light-emitting diodes simultaneously (Fig. 5e). Additionally, the Ce-BT-40//CeNiCo-LDH ASC devices exhibited an impressive capacitance retention of 91.4% and a Coulombic efficiency close to 100% after 3800 charge/discharge cycles. These outstanding performances highlight the potential of the prepared ASC devices for diverse applications, especially in situations where space is limited.

3. Conclusions

In summary, Ce-doped BT was synthesized as an ASC anode material in one step using a simple and rapid microwave-assisted solvothermal method. Ce doping not only generates abundant amorphous regions to enhance the electrical conductivity but also induces the formation of nanoflowers globular morphology structure to improve the comparative area and porosity. The electrochemical test results show that Ce doping significantly enhances the electrochemical performance of BT. Specifically, the obtained Ce-BT-40 electrode has a specific capacitance of 721 F g⁻¹ at 0.5 A g⁻¹ and is still able to maintain 587 F g⁻¹ at 10 A g⁻¹. To evaluate the practicality of Ce-BT-40, ASC device was fabricated using the as-prepared Ce-BT-40 and CeNiCo-LDH. The fabricated ASC device provides 59.1 Wh kg⁻¹ at 652 W kg⁻¹. This work not only revealed the mechanism of the effect of Ce doping on the electrochemical properties of Bi₂O₃ but also proposed a microwave-assisted solvent method to realize the rapid synthesis of electrode materials, which provides a new idea for the development of high energy density and low-cost ASCs.

CRedit authorship contribution statement

X. Tao, M.Q. Wei : Conception and design of the study. **B.C. Zhang** : Acquisition of data. **L.L. Zhang, R.L. Zhu** : Analysis and/or interpretation of data. **L.Han, G.Z. Zhao, Y.Y. Zhu** : Visualization, Investigation. **H.L. Jin, G. Zhu** : Validation, Formal analysis, Funding Support. **L.H. Yu** : Writing-review & editing.

Data availability

Data will be made available on request.

Acknowledgments

This study was financially supported by the Provincial Natural Science Foundation of Anhui (1908085ME120), Research Project of Education Department of Anhui Province (2023AH052221, 2023AH052230, 2023AH052247), Excellent Young Talents in Universities of Anhui Province (Grant No. 2022AH030134) and the Doctor of Suzhou University Scientific Research Foundation Project (No. 2020BS014) for the financial support of this research.

References

1. S. Shahriar, T. Erkan, When will fossil fuel reserves be diminished? *Energy Policy* 37 (2009) 181-189.
2. E. Vinodkumar, M. Rotem, E. Ran, S. Gregory, A. Doron, Challenges in the development of advanced Li-ion batteries: a review, *Energy Environ. Sci.* 4 (2011) 3243-3262.
3. S. Chu, Y. Cui, N. Liu, The path towards sustainable energy, *Nat. Mater.* 16 (2017) 16-22.
4. H. Liu, X. Liu, S. Wang, H. Liu, L. Li, Transition metal based battery-type electrodes in hybrid supercapacitors: A review, *Energy Storage Mater.* 28 (2020) 122-145.
5. K. Zhang, X. Han, Z. Hu, X. Zhang, Z. Tao, J. Chen, Nanostructured Mn-based oxides for electrochemical energy storage and conversion, *Chem. Soc. Rev.* 44 (2015) 699-728.
6. N. Choudhary, C. Li, J. Moore, N. Nagaiah, L. Zhai, Y. Jung, J. Thomas, Asymmetric supercapacitor electrodes and devices, *Adv. Mater.* 29 (2017) 1605336.
7. A. Amiri, A. Bruno, A. Polycarpou, Configuration-dependent stretchable all-solid-state supercapacitors and hybrid supercapacitors, *Carbon Energy* 5 (2023) DOI:10.1002/cey2.320.
8. G. Pacchioni, Sustainable flexible supercapacitors, *Nat. Rev. Mater.* 7 (2022) 844-844.
9. M. Yu, Z. Wang, Y. Han, Y. Tong, X. Lu, S. H. Yang, Recent progress in the development of anodes for asymmetric supercapacitors, *J. Mater. Chem. A* 4 (2016) 4634-4658.

10. Q. Lu, B. Zi, Q. Lu, M. Chen, J. Zhang, Z. Zhu, Q. Liu, A brand-new hybrid structure with advantageous electron state for ultrahigh energy density asymmetric supercapacitors, *ACS Energy Lett.* 7 (2022) 4204-4214.
11. H. Gao, Y. Wang, H. Shen, Z. Wu, J. Song, J. Yu, H. Jing, P. Zhao, W. Lei, Q. Hao, Facial design and synthesis of Ce doped Co-Ni oxide nanocages with cubic structure for high-performance asymmetric supercapacitors, *Appl. Surf. Sci.* 615 (2023) 156132.
12. W. Yang, Y. Zhu, Z. Jia, L. He, L. Xu, J. Meng, M. Tahir, Z. Zhou, X. Wang, L. Mai, Interwoven nanowire based on-chip asymmetric microsupercapacitor with high integrability, areal energy, and power density, *Adv. Energy Mater.* 10 (2020) 2001873.
13. J. Yang, X. Xiao, P. Chen, K. Zhu, K. Cheng, K. Ye, G. Wang, D. Cao, J. Yan, Creating oxygen-vacancies in MoO_{3-x} nanobelts toward high volumetric energy-density asymmetric supercapacitors with long lifespan, *Nano Energy* 58 (2019) 455-465.
14. S. Zheng, Y. Fu, L. Zheng, Z. Zhu, J. Chen, Z. Niu, D. Yang, PEDOT-engineered Bi_2O_3 nanosheet arrays for flexible asymmetric supercapacitors with boosted energy density, *J. Mater. Chem. A* 7 (2019) 5530-5538.
15. Z. Yu, X. Zhang, L. Wei, X. Guo, MOF-derived porous hollow $\alpha\text{-Fe}_2\text{O}_3$ microboxes modified by silver nanoclusters for enhanced pseudocapacitive storage, *Appl. Surf. Sci.* 463 (2019) 616-625.
16. J. Zhao, Z. Li, T. Shen, X. Yuan, G. Qiu, Q. Jiang, Y. Lin, G. Song, A. Meng, Q. Li, Oxygen-vacancy Bi_2O_3 nanosheet arrays with excellent rate capability and CoNiS_4 nanoparticles immobilized on N-doped graphene nanotubes as robust electrode materials for high-energy asymmetric supercapacitors, *J. Mater. Chem. A* 7 (2019) 7918-7931.
17. Y. Liu, C. Chu, Y. Li, P. Deng, Y. Liu, R. Wu, X. Liu, Y. Zheng, W. Zhang, J. Wu, H. Li, Z. Kang, Enhanced supercapacitor performance of Bi_2O_3 by Mn doping. *J. Alloys Compd.* 914 (2022) 165258.
18. J. Chang, W. Liang, W. Wang, D. Wu, K. Jiang, G. Wang, F. Xu, Z. Gao, Oxygen vacancies enriched Bi_2O_3 as high capacity and high rate negative material for aqueous alkali battery, *Appl. Surf. Sci.* 601 (2022) 1542996.
19. D. Maruthamani, S. Vadivel, M. Kumaravel, B. Saravanakumar, B. Paul, S. Dhar, A. Habibi-Yangjeh, A. Manikandan, G. Ranadiss, Fine cutting edge shaped Bi_2O_3 rods/reduced graphene oxide (RGO) composite for supercapacitor and visible-light photocatalytic applications, *J. Colloid Interface Sci.* 498 (2017) 449-459.
20. X. Yu, J. Sun, W. Zhao, S. Zhao, H. Chen, K. Tao, Y. Hu, L. Han, MOF-derived Bi_2O_3 @C microrods as negative electrodes for advanced asymmetric supercapacitor, *RSC Adv.* 10 (2020) 14107-14112.
21. S. Ghosh, S. Barg, S. Jeong, K. Ostrikov, Heteroatom-doped and oxygen-functionalized nanocarbons for high-performance supercapacitors, *Adv. Energy Mater.* 10 (2020) 2001239.
22. K. Yu, L. Lou, S. Liu, W. Zhou, Asymmetric oxygen vacancies: the intrinsic redox active sites in metal oxide catalysts, *Adv. Sci.* 7 (2020) 1901970.
23. F. Li, M. Cabral, B. Xu, Z. Cheng, E. Dickey, J. LeBeau, J. Wang, J. Luo, S. Taylor, W. Hackenberger, L. Bellaiche, Z. Xu, L. Chen, T. Shrout, S. Zhang, Giant piezoelectricity of Sn-doped $\text{Pb}(\text{Mg}_{1/3}\text{Nb}_{2/3})\text{O}_3$ - PbTiO_3 single crystals, *Science* 364 (2019) 264.
24. Y. Zhai, L. Xu, Y. Qian, Ce-doped $\alpha\text{-FeOOH}$ nanorods as high-performance anode material for energy storage, *J. Power Sources*, 327 (2016) 423-431.
25. S. Zai, X. Gao, C. Yang, Q. Jiang, Ce-modified $\text{Ni}(\text{OH})_2$ nanoflowers supported on NiSe_2 octahedra nanoparticles as high-efficient oxygen evolution electrocatalyst, *Adv. Energy Mater.* 11 (2021) 2101266.
26. L. Xu, W. Zhou, S. Chao, Y. Liang, X. Zhao, C. Liu, J. Xu, Advanced oxygen-vacancy Ce-doped MoO_3 ultrathin nanoflakes anode materials used as asymmetric supercapacitors with ultrahigh energy density, *Adv. Energy Mater.* 12 (2022) 2200101.
27. X. Li, N. Qian, L. Ji, X. Wu, J. Li, J. Huang, Y. Yan, D. Yang, H. Zhang, Enhanced electrocatalytic reduction of CO_2 to formate via doping Ce in Bi_2O_3 nanosheets, *Nanoscale Adv.* 4 (2022) 2288-2293.
28. N. Sun, B. Yin, D. Dong, X. Hu, Y. Huan, T. Wei, Revealing the intrinsic effects of introduced carbon nanotubes for Bi_2O_3 energy storage materials, *Electrochim. Acta* 409 (2022) 139948.
29. S. Li, D. Bao, M. Shi, B. Wulan, J. Yan, Q. Jiang, Amorphizing of Au nanoparticles CeO_x -RGO hybrid

- support towards highly efficient electrocatalyst for N_2 reduction under ambient conditions, *Adv. Mater.* 29 (2017) 1700001.
30. L. Xu, Y. Zhang, W. Zhou, F. Jiang, H. Zhang, Q. Jiang, Y. Jia, R. Wang, A. Liang, J. Xu, X. Duan, Fused heterocyclic molecule-functionalized N-doped reduced graphene oxide by non-covalent bonds for high-performance supercapacitors, *ACS Appl. Mater. Interfaces*, 12 (2020) 45202-45213.
 31. Z. Yu, S. Wang, Y. Huang, Y. Zou, F. Xu, C. Xiang, J. Zhang, J. Xie, L. Sun, Bi_2O_3 nanosheet-coated $NiCo_2O_4$ nanoneedle arrays for high-performance supercapacitor electrodes, *J. Energy Storage* 55 (2022) 105486.
 32. Q. Wu, S. Zhao, L. Yu, X. Zheng, Y. Wang, L. Yu, C. Nan, G. Cao, Oxygen vacancy-enriched MoO_{3-x} nanobelts for asymmetric supercapacitors with excellent room/low temperature performance, *J. Mater. Chem. A* 7 (2019) 13205-13214.
 33. M. Nagaraju, B. Ramulu, S. Arbaz, J. Yu, Facile one-step synthesized hierarchical $Bi_2O_3/Bi_{12}Mn_{12}O_{44}$ composite as a long-term stable and high-performance electrode for hybrid supercapacitors, *J. Alloys Compd.* 947 (2023) 169490.
 34. J. Yan, C. Ren, K. Maleski, C. Hatter, B. Anasori, P. Urbankowski, A. Sarucheva, Y. Gogotsi, Flexible MXene/Graphene films for ultrafast supercapacitors with outstanding volumetric capacitance, *Adv. Funct. Mater.* 27 (2017) 1701264.
 35. X. Yang, C. Cheng, Y. Wang, L. Qiu, D. Li, Liquid-mediated dense integration of graphene materials for compact capacitive energy storage, *Science* 341 (2013) 534-537.
 36. X. Zhang, W. Lu, Y. Tian, S. Yang, Q. Zhang, D. Lei, Y. Zhao, Nanosheet-assembled $NiCo$ -LDH hollow spheres as high-performance electrodes for supercapacitors, *J. Colloid Interface Sci.* 606 (2022) 1120-1127.
 37. M. Dinari, H. Allami, M. Momeni, Construction of Ce-doped $NiCo$ -LDH@CNT nanocomposite electrodes for high-performance supercapacitor application, *Energy Fuel* 35 (2021) 1831-1841.
 38. Y. Liao, R. He, W. Pan, Y. Li, Y. Wang, J. Li, Y. Li, Lattice distortion induced Ce-doped $NiFe$ -LDH for efficient oxygen evolution, *Chem. Eng. J.* 464 (2023) 142669.
 39. K. Qwusu, Z. Wang, A. Saad, F. Boakye, M. Mushtaq, M. Tahir, G. Yasin, D. Liu, Z. Peng, X. Cai, Room temperature synthesis of vertically aligned amorphous ultrathin $NiCo$ -LDH nanosheets bifunctional flexible supercapacitor electrodes, *Energy Environ. Mater.* (2023) DOI: 10.1002/eem2.12545.
 40. S. Mane, A. Kashale, G. Kamble, S. Kolekar, S. Dhas, M. Patil, A. Moholkar, B. Sathe, Facile synthesis of flower-like Bi_2O_3 as an efficient electrode for high performance asymmetric supercapacitor, *J. Alloys Compd.* 926 (2022) 166722.
 41. S. Yang, L. Qian, Y. Ping, H. Zhang, J. Li, B. Xiong, P. Fang, C. He, Electrochemical performance of Bi_2O_3 supercapacitors improved by surface vacancy defects, *Ceram. Int.* 47 (2021) 8290-8299.
 42. M. Paliwal, S. Meher, Sedgeli-like porous Co_3O_4 nanoarrays as a novel positive electrode material for Co_3O_4 parallel to Bi_2O_3 Asymmetric supercapacitors, *ACS Appl. Nano Mater.* 2 (2019) 5573-5586.

Hosted file

Figures-png\begin{CJK}{UTF8}{gbsn}.\end{CJK}\selectlanguage{english}.docx available at <https://authorea.com/users/671749/articles/671145-facile-microwave-assisted-synthesis-of-ce-doped-bi2o3-for-efficient-asymmetric-supercapacitors>